

# Enhanced Performance of Alkali Metal Doped $\text{Fe}_2\text{O}_3$ and $\text{Fe}_2\text{O}_3/\text{Al}_2\text{O}_3$ Composites As Oxygen Carrier Material in Chemical Looping Combustion

Lu Liu and Michael R. Zachariah\*

Department of Chemical and Biomolecular Engineering and Department of Chemistry and Biochemistry, University of Maryland, College Park, Maryland 20742, United States

## S Supporting Information

**ABSTRACT:** In this study alkali metal doped  $\text{Fe}_2\text{O}_3$  and  $\text{Fe}_2\text{O}_3/\text{Al}_2\text{O}_3$  composite oxygen carriers were synthesized from spray pyrolysis, and the reactivity and stability as oxygen carrier materials were evaluated in a fixed bed reactor for 50 isothermal redox cycles using  $\text{CH}_4$  as the fuel. We find that both  $\text{Fe}_2\text{O}_3$  and  $\text{Fe}_2\text{O}_3/\text{Al}_2\text{O}_3$  composite showed reactivity degradation over multiple cycles, with a clear phase separation between Fe and Al, in the composites. In contrast, alkali metal doping ( $\sim 5$  mol %) with Na, K, and Cs was found to stabilize the reactivity of the  $\text{Fe}_2\text{O}_3$  over the 50 redox cycles and prevent phase Fe–Al separation in the composite. Methane to  $\text{CO}_2$  selectivity was found to be relevant to the dopant type, which decreased in the order of dopant type K, Cs, and Na. The best performing alkali metal, K, enhanced long-term stability significantly, with no observed degradation in kinetics and total conversion performance in the methane step as well as reduced coke formation. Adding an alumina matrix to K doped  $\text{Fe}_2\text{O}_3$  helped promote  $\text{CO}_2$  generation as well as minimize coking and was found to be the best performing material.

## 1. INTRODUCTION

Chemical looping combustion (CLC) involves a two-step process in which metal oxides as the oxygen carrier (OC) replacing air in order to avoid direct contact between fuel and air.<sup>1</sup> Current primary interests in CLC lie in the potential advantages of burning hydrocarbons or coal in a nitrogen-free environment so as to enable more efficient/economical  $\text{CO}_2$  sequestering as well as avoid  $\text{NO}_x$  formation.<sup>2,3</sup> However, finding good oxygen carriers is one of the major challenges in any widespread implementation of CLC.<sup>4</sup> The important properties of oxygen carriers are high reactivity to both reduction and oxidation as well as high mechanical stability and recyclability over multiple cycles, low cost, and environmentally benign.<sup>5,6</sup> Metal oxides including copper-, iron-, nickel-, and mixed-oxide have been studied; however, Fe-based oxygen carriers while economical have shown a relatively slow reduction rate and a propensity for physical and chemical degradation over time.<sup>7–9</sup>  $\text{Fe}_2\text{O}_3$  can be sequentially reduced to  $\text{Fe}_3\text{O}_4$ , FeO, and finally Fe, with different  $\text{CO}_2$  conversions.<sup>10,35</sup> The economic advantages of an iron-based material coupled with its high melting point and being environmentally benign have continued to maintain interest in these materials. In an effort to enhance an active surface area, pore volume, sintering resistance, long-term stability and recyclability, support materials including  $\text{Al}_2\text{O}_3$ ,  $\text{SiO}_2$ , MgO,  $\text{TiO}_2$ ,  $\text{ZrO}_2$ , and  $\text{CeO}_2$  have been employed.<sup>4,9–12,32,33</sup> The performance improvement with supported OCs was often attributed to enhanced intraparticle gaseous diffusivity as well as electronic or  $\text{O}^{2-}$  mobility considering the reactions between OC and fuel are gas–solid or solid–solid reactions.<sup>13–15</sup>

In order to enhance the reactivity of  $\text{Fe}_2\text{O}_3$ , we have referred to the fact that alkali metal doping of catalysts has been known to improve selectivity and activity or prolong the lifetime of metal/metal oxide catalysts.<sup>16,21,24</sup> Specifically, activity de-

creases in the order of Cs, K, Na, and Li, attributed to the decreasing size, polarization, and electronegativity.<sup>23</sup> While strictly speaking the oxygen carrier is considered a reactant and not a catalyst, one might expect that some of the same principles that improve the catalyst may also improve oxidation performance. With that logic, in this study we demonstrate that K doped  $\text{Fe}_2\text{O}_3$  offers significant improvement in performance, both cycling and a lower coke formation potential in the reduction step with methane, while other alkali metals are not as effective. Further enhancement is seen when alumina is included to make composite alkali doped particles. In both cases, no long-term degradation in performance is observed.

## 2. APPROACH

All oxygen carriers studied were in-house synthesized by aerosol spray pyrolysis.<sup>26</sup> Briefly speaking, the system consists of an atomizer (to produce aerosol droplets), silica-gel diffusion drier (to remove solvent), a high temperature furnace, and a sample collector (to collect nanoparticles). The aerosol of precursor solution is generated using a collision-type nebulizer with an initial droplet diameter is about  $1 \mu\text{m}$ , which is dried by passing through a diffusion dryer. The aerosol is then passed through a tube furnace operated at  $600^\circ\text{C}$  to create the solid particle with a residence time of  $\sim 1$  s. Particles exiting the aerosol reactor are then collected on a  $0.4 \mu\text{m}$  DTTTP Millipore filter. In order to thermally decompose all nitrates completely, all particles were annealed at  $750^\circ\text{C}$  for 1 h before the CLC test.

The precursors for the  $\text{Fe}_2\text{O}_3$ ,  $\text{Al}_2\text{O}_3$ , and alkali metal components were  $\text{Fe}(\text{NO}_3)_3 \cdot 9\text{H}_2\text{O}$ ,  $\text{Al}(\text{NO}_3)_3 \cdot 9\text{H}_2\text{O}$ , and  $\text{MNO}_3$  ( $\text{M} = \text{Na}, \text{K}, \text{Cs}$ ), respectively, at a total concentration of 0.2 M. For the samples tested in this paper, a 5 mol % of alkali metal relative to Fe was added, in each case, such as 4.8 mol % K, 95.2 mol %  $\text{Fe}_2\text{O}_3$  ( $\text{Fe}_2\text{O}_3/\text{K}$ ), 4.8 mol % Cs,

Received: April 23, 2013

Revised: June 28, 2013

Published: July 8, 2013



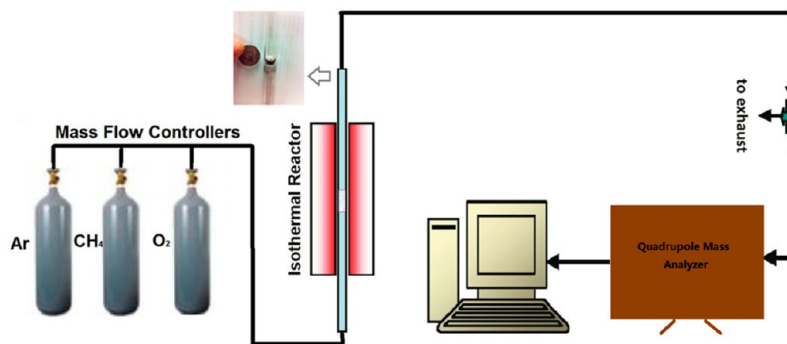


Figure 1. Schematic diagram of the CLC system.

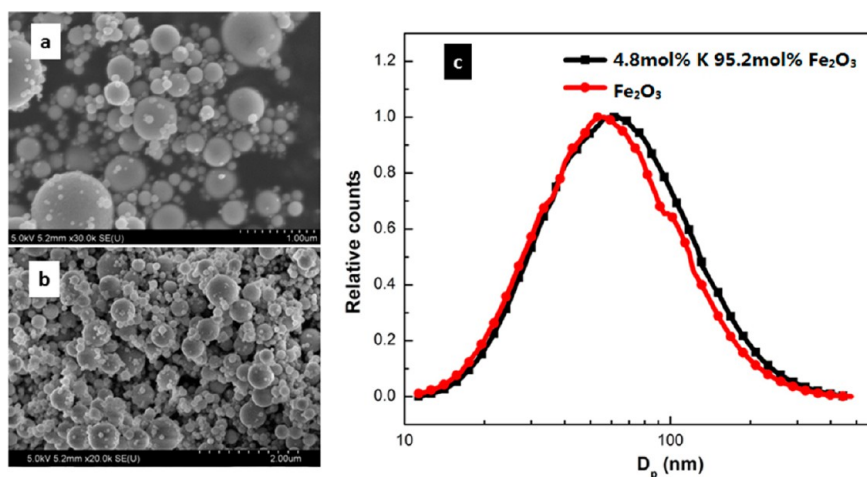


Figure 2. SEM images and particle-size distributions of as-synthesized  $\text{Fe}_2\text{O}_3$  (a) and 4.8 mol % K 95.2 mol %  $\text{Fe}_2\text{O}_3$  (b) produced by spray pyrolysis measured using a differential mobility analyzer (DMA) coupled with a condensation particle counter (CPC).

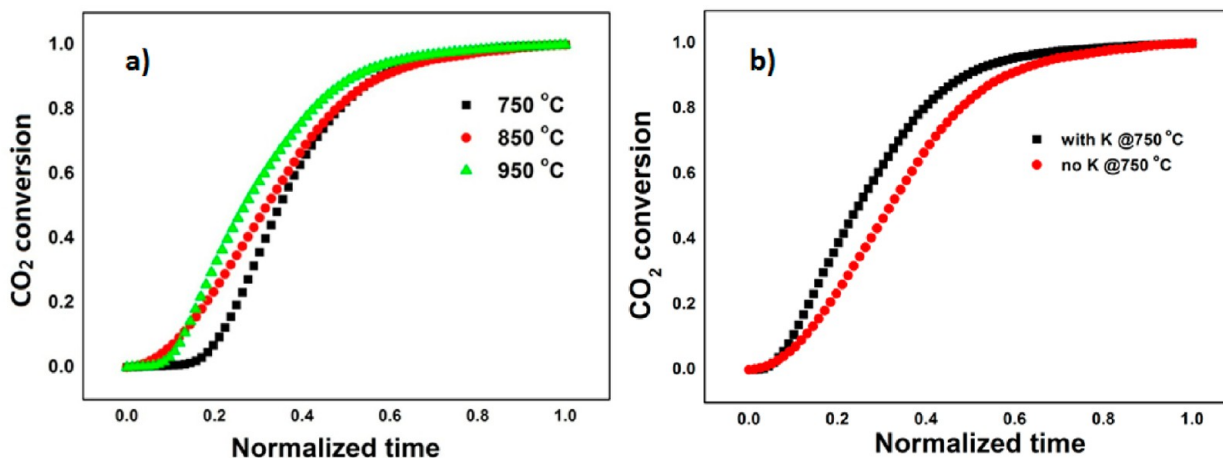
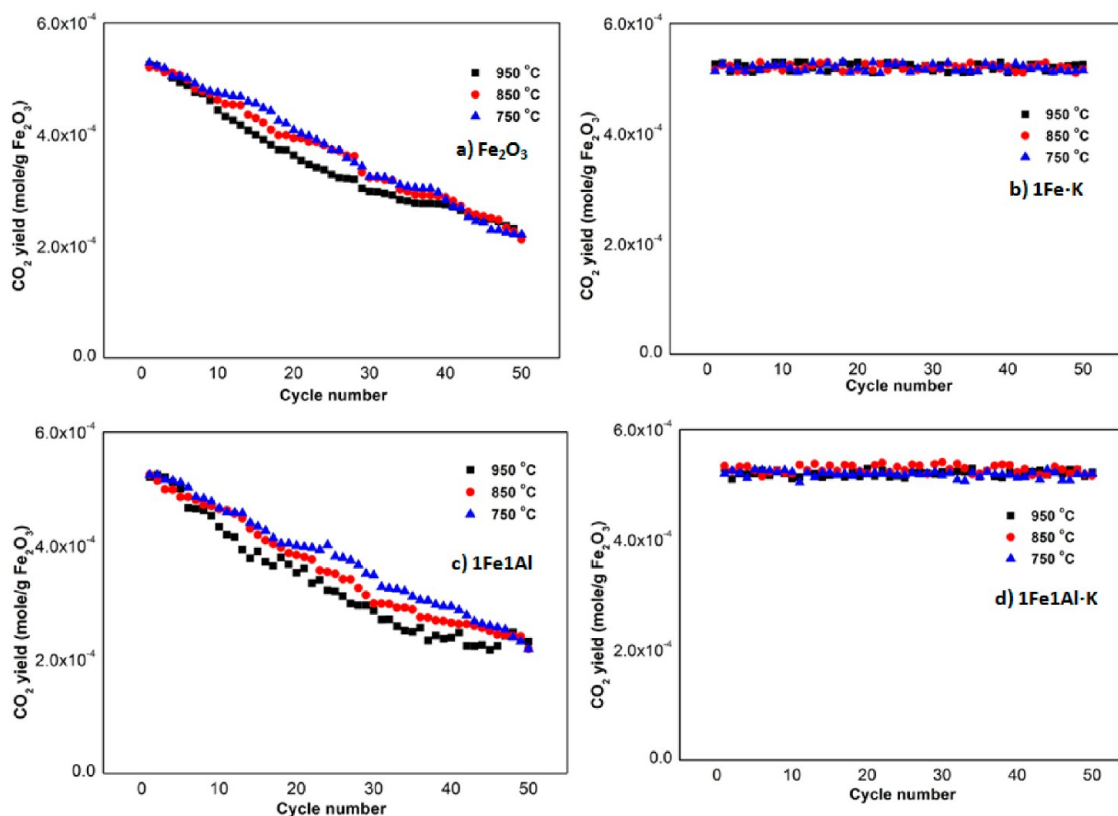


Figure 3. (a) Effect of temperature on temporal  $\text{CO}_2$  conversion for the 1st cycles of  $\text{Fe}_2\text{O}_3$  in the  $\text{CH}_4$  step and (b) comparison of potassium added vs neat iron oxide  $\text{CO}_2$  temporal conversion for the 1st cycle  $\text{CH}_4$  step at  $750\text{ }^\circ\text{C}$ .

95.2 mol %  $\text{Fe}_2\text{O}_3$  ( $\text{Fe}_2\text{O}_3\text{-Cs}$ ), 50 mol %  $\text{Fe}_2\text{O}_3/50$  mol %  $\text{Al}_2\text{O}_3$  (1Fe1Al), 2.6 mol % K, 48.7 mol %  $\text{Fe}_2\text{O}_3/48.7$  mol %  $\text{Al}_2\text{O}_3$  (1Fe1Al-K), 2.6 mol % Na, 48.7 mol %  $\text{Fe}_2\text{O}_3/48.7$  mol %  $\text{Al}_2\text{O}_3$  (1Fe1Al-Na), 1.3 mol % Na, 1.3 mol % Na, 48.7 mol %  $\text{Fe}_2\text{O}_3/48.7$  mol %  $\text{Al}_2\text{O}_3$  (1Fe1Al-1K1Na).

The reactivity of oxygen carriers was tested in a vertically oriented fixed bed reactor placed in an electrically heated isothermal furnace. While industrial practice probably favors the use of fluidized-beds, there are examples of designs for full scale fixed bed reactors for

CLC.<sup>27,28</sup> From a laboratory stand-point, fixed bed studies are widely used due to the simplicity of operation and the small samples that can be utilized.<sup>7,12,31,32,37,40</sup> This latter point was of particular interest to us since our focus is on materials synthesis and rapid screening. Readers will also note that our materials are nanoscale. Obviously this length scale is not practical in fluidized beds, however particles of the type described here are easily generated by spray pyrolysis methods at various sizes.<sup>29</sup> Finally it is possible to construct microsized particles comprised of nanoparticles by spray induced aggregation that offers



**Figure 4.** CO<sub>2</sub> yield per gram of Fe<sub>2</sub>O<sub>3</sub> for (a) Fe<sub>2</sub>O<sub>3</sub>, (b) Fe<sub>2</sub>O<sub>3</sub>-K (95.2 mol % Fe<sub>2</sub>O<sub>3</sub> with 4.8 mol % K), (c) 1Fe1Al (50 mol % Fe<sub>2</sub>O<sub>3</sub>/50 mol % Al<sub>2</sub>O<sub>3</sub>), (d) 1Fe1Al-K (2.6 mol % K 48.7 mol % Fe<sub>2</sub>O<sub>3</sub>/48.7 mol % Al<sub>2</sub>O<sub>3</sub>) at 750 °C, 850 °C, and 950 °C.

accessible surface areas that greatly exceed the corresponding external surface area.<sup>30</sup>

About 200 mg of sample material was used for each test. The quartz flow reactor has a length of 61 cm, with a 1 cm i.d. as described in Figure 1. The particles were first annealed at the reaction temperature for 1 h and then exposed alternatively to 11% methane for 2 min and 20% oxygen for 5 min simulating the CLC system. Argon is introduced for 300 s after each period to avoid oxygen and methane mixing during the shift between oxidation and reduction. In total, 50 cycles were achieved in this test.

MKS mass flow controllers (MFCs) for the three gases were regulated by a Labview VI program. The reactor effluent was characterized by a mass spectrometer (Stanford Research UGA 300) operating with a mass resolution <0.5 atomic mass unit (amu) at 10% of peak height and a detection limit <1 ppm. Argon was used as an inert internal standard to determine the volume change of gaseous reactants and products during the reaction so as to assign concentrations. By varying the flow rates of CH<sub>4</sub> and O<sub>2</sub> with a fixed Ar flow rate, calibrations of the mass spectrometer for different gases with different concentrations were accomplished. Crystal structures of OCs were characterized by X-ray diffraction (XRD) with a Bruker Smart1000 using Cu K $\alpha$  radiation. Transmission electron microscopy (TEM) and elemental mapping were performed using a field-emission transmission electron microscope (JEOL JEM 2100F). Scanning electron microscopy (SEM) and energy-dispersive X-ray (SEM-EDX) results were obtained by Hitachi SU-70 SEM.

### 3. RESULTS AND DISCUSSION

A differential mobility analyzer (DMA) coupled with a condensation particle counter (CPC) described in our previous work was utilized to obtain the size distribution of the as-synthesized particles.<sup>31</sup> As shown in Figure 2c, the Fe<sub>2</sub>O<sub>3</sub> particle diameter peaks at 84 nm without K and 87 nm with 5 mol % K, implying that particle size effects can be ignored in

any comparison. Similar results were obtained with other dopants (Na, Cs).

The multiple-cycle test in the fixed bed reactor examines the reactivity and stability of the selected oxygen carriers. Figure 3a illustrates the temporal dependence of oxygen carrier reduction with the CH<sub>4</sub> reaction to CO<sub>2</sub> of neat Fe<sub>2</sub>O<sub>3</sub> sample at the first cycles. Normalized time is the real time normalized by the pulse length. The conversion–time plot shows a sigmoidal shape, indicating that the gas–solid reaction may proceed following the JMA model.<sup>17,18</sup> Since this study primary focuses on total yield, selectivity, and cycling stability, the data presented subsequently are under conditions of steady conditions (i.e., long times) so that temperature dependence of kinetics cannot be evaluated. Figure 3b shows that adding potassium results in a slight improvement in the kinetics without changing final yield. This is important since any long-term stability improvements through the addition of potassium should not ultimately degrade kinetic performance. Assuming that both cases share the same reaction order, the temporal conversion plots yield a reaction rate for the potassium added case roughly twice that for the neat iron oxide.

Figure 4 shows the performance behavior at different temperatures for unmixed (Figure 4a,c) and K added OCs' multicycle performance (Figure 4b,d). Theoretically, the conversion from Fe<sub>2</sub>O<sub>3</sub> to Fe<sub>3</sub>O<sub>4</sub> should give a CO<sub>2</sub> yield of 0.52 mmol/g from Fe<sub>2</sub>O<sub>3</sub> to FeO, 1.56 mmol/g and from Fe<sub>2</sub>O<sub>3</sub> to Fe, 4.69 mmol/g. Equilibrium calculation shows that Fe<sub>2</sub>O<sub>3</sub> to Fe<sub>3</sub>O<sub>4</sub> under methane leads to 100% CO<sub>2</sub> but that subsequent partial reduction to FeO gives a mixture of CO and CO<sub>2</sub>.<sup>11,35</sup> Our experimental results could not reliably quantify this point due to relative high mass 28 (N<sub>2</sub>) background in our

mass spectrometer. It is clear that for the first cycle of the neat  $\text{Fe}_2\text{O}_3$  (Figure 4a) and 50 mol %  $\text{Fe}_2\text{O}_3$ /50 mol %  $\text{Al}_2\text{O}_3$  (Figure 4c) samples, the  $\text{Fe}_2\text{O}_3$  got converted to  $\text{Fe}_3\text{O}_4$  after the  $\text{CH}_4$  step. Also, it demonstrates that from Figure 4a that for pure  $\text{Fe}_2\text{O}_3$ , performance degrades steadily after each cycle, which has also been reported by others and is one of the problems plaguing many OCs.<sup>25</sup> Addition of aluminum nitrate to create an alumina stabilizing matrix (Figure 4c) for the  $\text{Fe}_2\text{O}_3$  exhibited essentially identical behavior to the neat  $\text{Fe}_2\text{O}_3$  oxide case, implying that at least under the synthetic strategy pursued here, the alumina offered no advantages. For both cases before  $\text{K}^+$  addition (Figure 4a,c),  $\text{CO}_2$  generation degraded to almost one-third its first cycle at the 50th cycle. The addition of K however, shown in Figure 4b,d stabilized the performance even up to 950 °C, with no temperature dependence to the conversion or stability over the 50 cycles studied. At various loadings, 80 mol %  $\text{Fe}_2\text{O}_3$  20 mol %  $\text{Al}_2\text{O}_3$ , 67 mol %  $\text{Fe}_2\text{O}_3$  33 mol %  $\text{Al}_2\text{O}_3$  OCs were also tested, with no difference in performance detected. The degradation may be attributed to the decreasing oxygen-ion transport within the lattice or a reduction in the oxygen binding energy.<sup>20</sup> Meanwhile, adding  $\text{K}^+$  to the  $\text{Fe}_2\text{O}_3$ / $\text{Al}_2\text{O}_3$  composite also helped modify the degradation problem (Figure 4d). To be more specific, 2.6 mol % K 48.7 mol %  $\text{Fe}_2\text{O}_3$  48.7 mol %  $\text{Al}_2\text{O}_3$  OC also gave a steady  $\text{CO}_2$  yield of  $\text{Fe}_2\text{O}_3$  to  $\text{Fe}_3\text{O}_4$  as the  $\text{Fe}_2\text{O}_3$  case during those 50 cycles. What is responsible for this effect will be specified later in this paper.

Next we turn to the effects of alkali metals as dopants. To compare the effects of different alkali doping, we chose to use Na, K, and Cs to vary the size, polarization, and electronegativity of the dopant. Plots of the  $\text{CO}_2$  yields per gram of  $\text{Fe}_2\text{O}_3$  for different oxygen carriers (OCs) for 50 redox cycles is presented in Figure 5. The first thing to note is that addition of

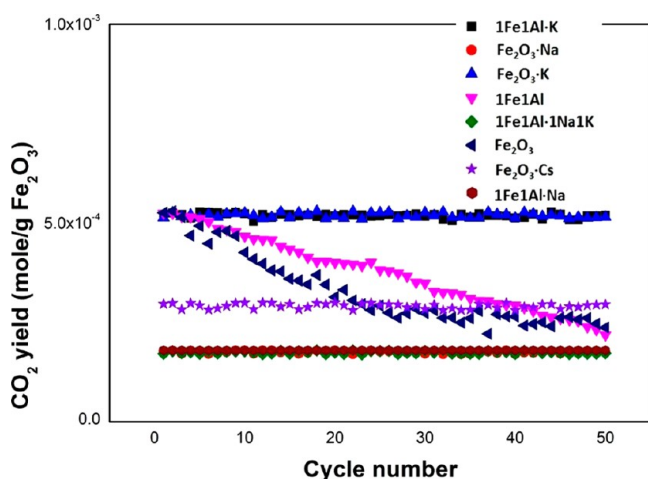
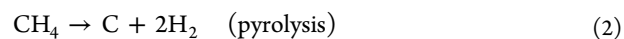


**Figure 5.**  $\text{CO}_2$  yield per gram of  $\text{Fe}_2\text{O}_3$  for different OCs at 750 °C as a function of cycle number.

the alkali metal dopant clearly stabilizes the long-term stability of the  $\text{CO}_2$  conversion with no apparent decreases in performance over time, but only K offers high oxygen transport capacity for iron oxide. Usually, alkaline ions are considered as catalysts; however, they only prevent performance degradation instead of improving performance compared to the neat  $\text{Fe}_2\text{O}_3$  initially in our case. Alkaline metals are thought to act as an electron donor for the iron based materials and that the synergistic effects are ascribed to the weakening of the Fe–O

bond.<sup>19,20</sup> The Na added OC sample showed the worst performance, which can be attributed to its smaller radius and lower electronegativity, consistent with previous work on the role of alkaline metals on catalytic activity.<sup>23</sup> On that basis, however, Cs should perform better than K but clearly did not. TEM images of reacted OCs (Figures S2 and S3 in the Supporting Information) show that Cs was not retained after thermal processing (at least at significant levels within the iron oxide lattice) but phase-separated into small primary particles decorating the surface (TEM-EDX identified that metal elements of the small grains on the bulk  $\text{Fe}_2\text{O}_3$  surface are mainly Cs), possibly because of the increased atom size. Alkali metals have also been shown to improve selectivity, reduce coking, or prolong lifetime of metal/metal oxide catalysts for various reactions.<sup>19–24</sup> At least for the conversion, addition of aluminum oxide stabilizer appears to be no advantage, but it is included here because of a subsequent discussion on selectivity.

Because one of the primary motivations of CLC today is  $\text{CO}_2$  sequestering, selectivity is extremely important, specifically with respect to coking, which may occur from a number of side reactions including the Boudouard reaction (reaction 1) and methane pyrolysis (reaction 2).<sup>34–37</sup>



The second reaction is endothermic while the first reaction is exothermic. Furthermore, methane decomposition is thermodynamically preferred at high temperatures, while the Boudouard reaction is favored at low temperatures. Carbon formation comes from the two reactions mentioned above and then burned away in the oxidation step.<sup>37–39</sup> Therefore, the amount of  $\text{CO}_2$  observed in the oxidation step can be directly used to determine the extent of coke formation in the methane step. The two different side reactions can be differentiated by the amount of hydrogen generated during the methane step, as it results only from methane decomposition (reaction 2). As the amount of hydrogen generated during the methane step was double the amount of  $\text{CO}_2$  generated during the oxidation step, we can conclude that methane decomposition is the primary side reaction. We define  $\text{CO}_2$  selectivity (based on the amount of  $\text{CO}_2$  measured during the fuel step) as

$$\gamma_{\text{CO}_2} = \frac{n_{\text{CO}_2}}{n_{\text{C}} + n_{\text{CO}_2}}$$

where  $n_{\text{CO}_2}$  is determined directly during the fuel step, and  $n_{\text{C}}$  is measured indirectly by the amount of  $\text{CO}_2$  measured during the oxidation step. Thus, the selectivity represents the amount of methane that is reacting with the OCs rather than decomposing.  $\gamma_{\text{CO}_2}$  of different OCs at 750 °C for 50 cycles is shown in Figure 6. It is evident that addition of alkaline metals improves  $\text{CO}_2$  selectivity against coking and that potassium works best in the context of selectivity. The addition of the alumina support provides further improvement. This 48.7 mol %  $\text{Fe}_2\text{O}_3$ /48.7 mol %  $\text{Al}_2\text{O}_3$ /2.6 mol % K material clearly offers superior performance in both reactivity stability and  $\text{CO}_2$  selectivity. This result implies that alkali metals promote oxidation over pyrolysis although the mechanism is not well understood.

Phase identification of oxygen carriers was determined using XRD (Table S1 in the Supporting Information), indicating that all iron oxides were  $\gamma\text{-Fe}_2\text{O}_3$  or  $\text{Fe}_3\text{O}_4$ . Even though the samples

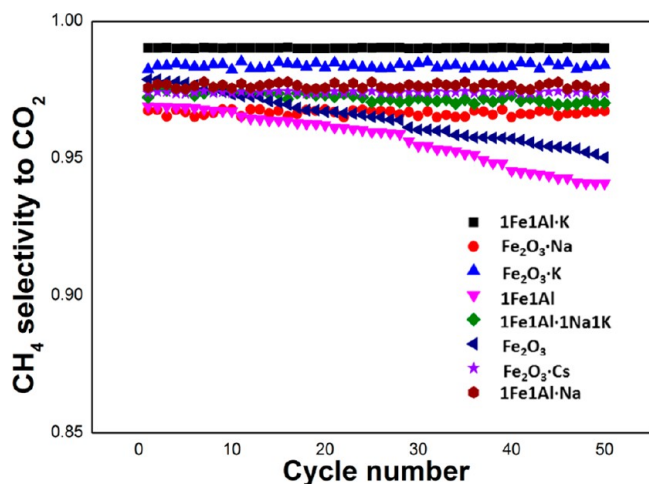


Figure 6.  $\text{CO}_2$  selectivity,  $\gamma_{\text{CO}_2}$  of different OCs at 750 °C.

were obtained after the  $\text{CH}_4$  step cooled down to room temperature in Ar, the high temperature reduced phase gets easily oxidized and thus all XRD patterns gave peaks assigned to  $\text{Fe}_2\text{O}_3$  and four reduced samples (OC samples after the  $\text{CH}_4$  step) gave peaks of  $\text{Fe}_3\text{O}_4$ . No signals for K–Fe–O may come from two reasons: (1) K–Fe forms very fine particles beyond the limit of XRD detection and (2) K–Fe forms solid solutions. From HR-TEM results (Figures S2 and S3 in the Supporting Information), the second one is more reasonable since K–Fe stayed homogeneously distributed in the particle. Also, the XPS and deconvolution results for the Fe 2p core-level (Figure S4 in the Supporting Information) of 4.8 mol % K 95.2 mol %  $\text{Fe}_2\text{O}_3$  sample showed very similar patterns and main peaks of Fe 2p<sub>3/2</sub> around 710.8 eV, which demonstrates no chemical bonding between K and Fe, which means that  $\text{K}^+$  may move around in

the  $\text{Fe}_2\text{O}_3$  crystal as ion interstitials. XRD analysis on the  $\text{Al}_2\text{O}_3$  supported sample has two major phases:  $\text{Fe}_2\text{O}_3$  and  $\text{Al}_2\text{O}_3$ , with no mixed Fe–Al–O phase formation and no mixed Fe–K–Al–O phase formation is detected (e.g.,  $\text{KFeO}_2$ ). Moreover, XPS also gave the same information.

The SEM micrographs of the OCs are shown in Figure 7. Consistent with the size distribution measurements in Figure 2, as produced particles from spray pyrolysis were spherical  $\sim 0.1$ – $1 \mu\text{m}$ . After  $\sim 1$  h thermal annealing at 750 °C, particles maintained their spherical shapes. After 50 cycles (15 h), particles clearly showed evidence of some sintering, although for all but the smallest particles the characteristic length scales are still nominally the same. The Na doped sample (not shown) was essentially indistinguishable from the K counterparts despite the fact that the reactivity was much lower. It is worth noticing that all particles displayed similar amounts of sintering, regardless of alkali metal doping. It can be implied that sintering does not account for the reactivity differences.

TEM elemental mapping is shown in Figures 8 and 9, for the as prepared 50 mol %  $\text{Fe}_2\text{O}_3$ /50 mol %  $\text{Al}_2\text{O}_3$  (Figure 8a,c), after multicycles at 750 °C (Figure 8b,d) and 2.6 mol % K 48.7 mol %  $\text{Fe}_2\text{O}_3$ /48.7 mol %  $\text{Al}_2\text{O}_3$  after multicycle CLC at 750 °C. Figure 8a,c show that in the as-produced material, the iron is homogeneously dispersed within the alumina matrix but that after CLC (Figure 8b,d), considerable morphological changes have occurred accompanied with a significant phase separation between Fe and Al. This is also consistent with the fact as shown in Figure 4 that the Al additions to iron oxide have minimal performance effects and show the same general trend of decreasing activity with time. However, 2.6 mol % K 48.7 mol %  $\text{Fe}_2\text{O}_3$ /48.7 mol %  $\text{Al}_2\text{O}_3$  composite, as shown in Figure 9, clearly stabilizes the structure from both morphological sintering effects but also phase separation between Al and Fe.

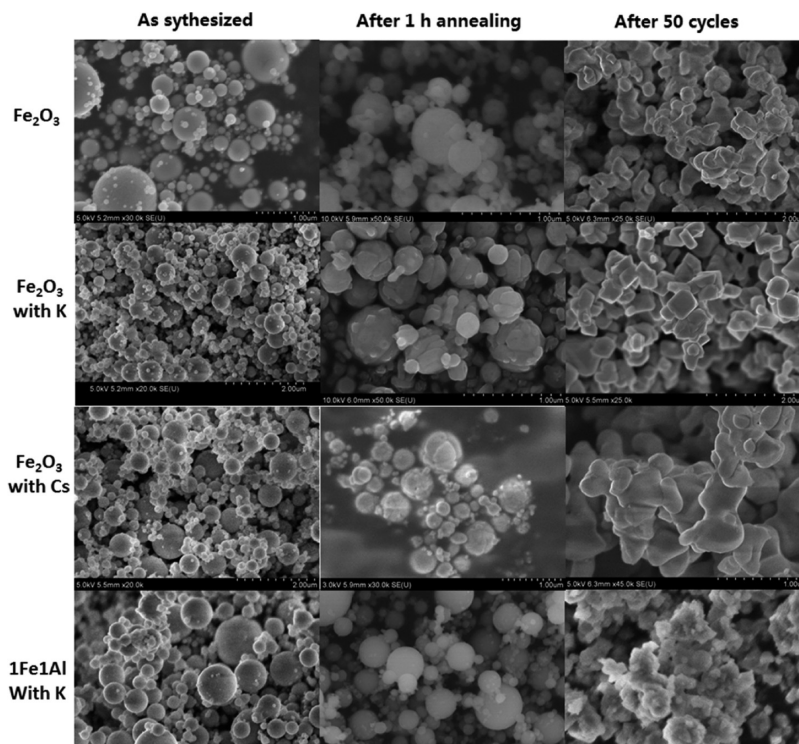
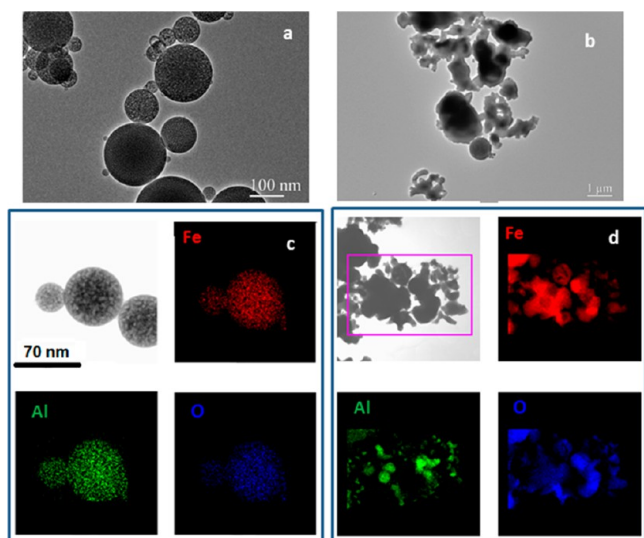
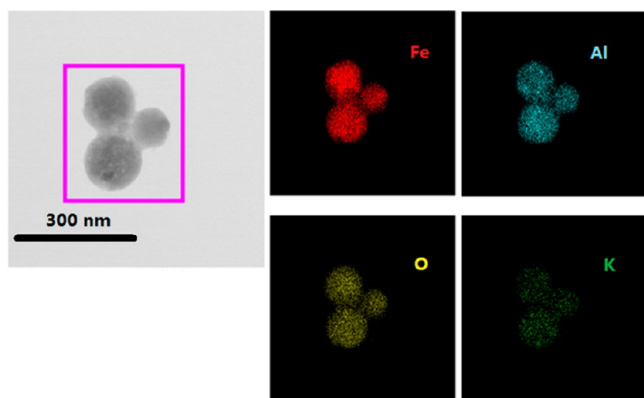


Figure 7. SEM images of OCs after direct synthesis, 1 h thermal annealing at 750 °C, and 50 cycles of CLC test at 750 °C.



**Figure 8.** TEM and elemental mapping results for 50 mol %  $\text{Fe}_2\text{O}_3$ /50 mol %  $\text{Al}_2\text{O}_3$ : (a,c) As synthesized and (b,d) after 50 CLC cycles at 750 °C.



**Figure 9.** TEM and elemental mapping: 48.7 mol %  $\text{Fe}_2\text{O}_3$ /48.7 mol %  $\text{Al}_2\text{O}_3$  with 2.6 mol % K after 50 CLC cycles at 750 °C.

Similar results (Figure S1 in the Supporting Information) were achieved with the Na sample after 50 cycles, but recall that the Na containing sample did not perform well. The mapping results indicate that the alkaline metal helps to retard phase separation within the alumina support, which may account for the long-term stability of 2.6 mol % K 48.7 mol %  $\text{Fe}_2\text{O}_3$ /48.7 mol %  $\text{Al}_2\text{O}_3$  OC relative to the nascent iron oxide and little alkaline metal loss. Potassium ions movement may exist as a binder for Fe–Al, thus preventing phase separation between the two. This result indicates that the alkaline effect here is more than the catalytic surface effect; it is a whole particle effect.<sup>39</sup> Additional TEM images in the Supporting Information (Figures S2 and S3) indicate that Cs, however, did not stay in iron oxide and was found to phase separate to the surface of the OC surface. This separation may be attributed to the larger size of the  $\text{Cs}^+$  (~181 pm) ion compared to  $\text{K}^+$  (~152 pm) and  $\text{Na}^+$  (~116 pm) as well its higher ion polarization.<sup>23–25,41</sup> Previous catalysis studies have seen similar trends in the tendency for Cs phase separation.<sup>16,21–24</sup>

Our experimental approach is not amenable to identify the root cause of the potassium effect; however, unlike a catalysis which is a pure surface effect, we are driving the OC within the whole particle and thus we expect whatever the alkali metal

effect it must involve more than surface effects. This may involve changing oxygen-ion transport within the lattice or a reduction in the oxygen binding energy. The fact that Na with its lower electronegativity performs worse is consistent with this, with the Cs, because of its instability within the lattice not providing any useful insights on this point. The stability of iron within the alumina implies that the alkali metal (both K and Na) stiffens the alumina matrix from moving around and offers a stable path for oxygen transport to the surface which may help to explain the improved selectivity (i.e., reduction in coking).

#### 4. CONCLUSIONS

We demonstrate that addition of potassium to iron oxide nanoparticles during synthesis can significantly enhance its performance in long-term CLC tests of methane oxidation. This was however not true for Na or Cs addition. In the latter, Cs addition was not incorporated within the lattice but was found to phase separate into small Cs particles at the surface of the iron oxide. Synthesis of particles with an alumina matrix was found to have a minimal effect for nascent iron oxide performance but when added in combination with potassium yielded the best performance in terms of long-term stability as well as  $\text{CO}_2$  selectivity with respect to coking.

#### ■ ASSOCIATED CONTENT

##### 📄 Supporting Information

XRD identifications of different OCs sample, TEM images, and XPS and deconvolution results. This material is available free of charge via the Internet at <http://pubs.acs.org>.

#### ■ AUTHOR INFORMATION

##### Corresponding Author

\*E-mail: [mrz@umd.edu](mailto:mrz@umd.edu).

##### Notes

The authors declare no competing financial interest.

#### ■ ACKNOWLEDGMENTS

The authors wish to thank our supporters and financiers, the United States Department of Energy (DOE).

#### ■ REFERENCES

- (1) International Energy Agency (IEA). In *World Energy Outlook 2008*; IEA Publications: Paris, France, 2008.
- (2) Richter, H.; Knoche, K. Reversibility of Combustion Processes. *ACS Symp. Ser.* **1983**, 71–85.
- (3) Bolh ar-Nordenkamp, J.; Pr oll, T.; Kolbitsch, P.; Hofbauer, H. Comprehensive Modeling Tool for Chemical Looping Based Processes. *Chem. Eng. Technol.* **2009**, 32, 410–417.
- (4) Ishida, M.; Zheng, D.; Akehata, T. Evaluation of a Chemical-Looping-Combustion Power-Generation System by Graphic Energy Analysis. *Energy* **1987**, 12, 147–154.
- (5) Lyngfelt, A.; Leckner, B.; Mattisson, T. A Fluidized-bed Combustion Process with Inherent  $\text{CO}_2$  Separation; Application of Chemical-Looping Combustion. *Chem. Eng. Sci.* **2001**, 56, 3101–3113.
- (6) Mattison, T.; Johansson, M.; Lyngfelt, A. Multicycle Reduction and Oxidation of Different Types of Iron Oxide Particles-Application to Chemical Looping Combustion. *Energy Fuels* **2004**, 18, 628–637.
- (7) Corbella, B.; Diego, L.; Garcia-Labiano, F.; Adanez, J.; Palacios, M. Characterization and Performance in a Multicycle Test in a Fixed-bed Reactor of Silica-supported Copper Oxide as Oxygen Carrier for Chemical Looping Combustion of Methane. *Energy Fuels* **2006**, 20, 148–154.

- (8) Yang, S.; Kim, K.; Baek, J.; Kim, J.; Lee, J.; Ryu, C.; Lee, G. Spinel Ni(Al, Fe)<sub>2</sub>O<sub>4</sub> Solid Solution as an Oxygen Carrier for Chemical Looping Combustion. *Energy Fuels* **2012**, *26*, 4617–4622.
- (9) Cho, P.; Mattisson, T.; Lyngfelt, A. Comparison of Iron-, Nickel-, Copper- and Manganese-Based Oxygen Carriers for Chemical Looping Combustion. *Fuel* **2004**, *83*, 1215–1225.
- (10) Abad, A.; García-Labiano, F.; de Diego, L. F.; Gayán, P.; Adánez, J. Reduction kinetics of Cu-, Ni- and Fe-based Oxygen Carriers Using Syngas (CO+H<sub>2</sub>) for Chemical Looping Combustion. *Energy Fuels* **2007**, *21*, 1843–1853.
- (11) Jerndal, E.; Mattisson, T.; Lyngfelt, A. Thermal Analysis of Chemical Looping Combustion. *Chem. Eng. Res. Des.* **2006**, *84*, 795–806.
- (12) Bhavsar, S.; Vesper, G. Reducible Supports for Ni-based Oxygen Carriers in Chemical Looping Combustion. *Energy Fuels* **2013**, *27*, 2073–2084.
- (13) Energy Information Administration (EIA). *International Energy Outlook 2010*, EIA, U.S. Department of Energy: Washington, DC, 2010.
- (14) Jiang, D.; Carter, E. Diffusion of Interstitial Hydrogen into and through BCC Fe from First principles. *Phys. Rev. B* **2004**, *70*, 064102/1–064102/9.
- (15) Li, F.; Luo, S.; Sun, Z.; Bao, X.; Fan, L. Role of Metal Oxide Support in Redox Reactions of Iron Oxide for Chemical Looping Applications: Experiments and Density Functional Theory Calculations. *Energy Environ. Sci.* **2011**, *4*, 3661–3667.
- (16) Huo, C.; Wu, B.; Gao, P.; Yang, Y.; Li, Y.; Jiao, H. The Mechanism of Potassium Promoter: Enhancing The Stability of Active Surfaces. *Angew. Chem., Int. Ed.* **2011**, *50*, 7403–7406.
- (17) Khawam, A.; Flanagan, D. Solid-state Kinetic Models: Basic and Mathematical Fundamentals. *J. Phys. Chem. B* **2006**, *110*, 17315–17328.
- (18) Monazam, E.; Siriwardane, R.; Breault, R.; Tian, H.; Shadle, L.; Richards, G.; Carpenter, S. Kinetics of the Reduction of CuO/bentonite by Methane (CH<sub>4</sub>) during Chemical Looping Combustion. *Energy Fuels* **2012**, *26*, 2779–2785.
- (19) Lee, S. B.; Weiss, M.; Ertl, G. Adsorption of Potassium on Iron. *Surf. Sci.* **1981**, *108*, 357–367.
- (20) Yu, Z.; Li, C.; Fang, Y.; Huang, J.; Wang, Z. Reduction Rate Enhancements for Coal Direct Chemical Looping Combustion with an Iron Oxide Oxygen Carrier. *Energy Fuels* **2012**, *26*, 2505–2511.
- (21) Figueiredo, R. T.; Santos, M. S.; Andrade, H. M. C.; Fierro, J. L. G. Effect of Alkali Cations on the Cu/ZnO/Al<sub>2</sub>O<sub>3</sub> Low Temperature Water Gas Shift Catalyst. *Catal. Today* **2011**, *172*, 166–170.
- (22) Weiss, W.; Ranke, W. Surface Chemistry and Catalysis on Well-defined Epitaxial Iron-Oxide Layers. *Prog. Surf. Sci.* **2002**, *70*, 1–151.
- (23) Mross, W. Alkali Doping in Heterogeneous Catalysis. *Catal. Rev. Sci. Eng.* **1983**, *25*, 591–637.
- (24) Wu, J.; Saito, M. Improvement of Stability of a Cu/ZnO/Al<sub>2</sub>O<sub>3</sub> Catalyst for the CO Shift Reaction. *J. Catal.* **2000**, *195*, 420–422.
- (25) Gu, H.; Shen, H.; Xiao, J.; Zhang, S.; Song, T. Chemical Looping Combustion of Biomass/coal with Natural Iron Ore as Oxygen Carrier in a Continuous Reactor. *Energy Fuels* **2011**, *25*, 446–455.
- (26) Wu, C.; Sullivan, K.; Chowdhury, S.; Jian, G.; Zhou, L.; Zachariah, M. Encapsulation of Perchlorate Salts within Metal Oxides for Application as Nanoenergetic Oxidizers. *Adv. Funct. Mater.* **2012**, *22*, 78–85.
- (27) Noorman, S.; van Sint Annaland, M.; Kuipers, H. Packed Bed Reactor Technology for Chemical Looping Combustion. *Ind. Eng. Res.* **2007**, *46*, 4212–4220.
- (28) Noorman, S.; van Sint Annaland, M.; Kuipers, H. Experimental Validation of Packed Bed Chemical Looping Combustion. *Chem. Eng. Sci.* **2010**, *65*, 92–97.
- (29) Kostas, T.; Mark, J. *Aerosol Processing of Materials*, 1st ed.; Wiley-VCH: New York, 1999.
- (30) Wang, H. Y.; Jian, G. Q.; Yan, S.; Delisio, J. B.; Huang, C.; Zachariah, M. R. Electrospray Formation of Gelled Nano-Aluminum Microspheres with Superior Reactivity. *ACS Appl. Mater. Interfaces* **2013**, DOI:10.1021/am401238t.
- (31) Jian, G.; Liu, L.; Zachariah, M. Facile Aerosol Route to Hollow CuO Spheres and its Superior Performance as an Oxidizer in Nanoenergetic Gas Generators. *Adv. Funct. Mater.* **2013**, *23*, 1341–1346.
- (32) Duane, M.; Ranjani, S. Mechanism of Methane Chemical Looping Combustion with Hematite Promoted with CeO<sub>2</sub>. *Energy Fuels* **2013**, DOI: 10.1021/ef302132e.
- (33) de Diego, L. F.; García-Labiano, F.; Adanez, J.; Gayan, P.; Abad, A.; Corbella, B.; Palacios, J. Development of Cu-based Oxygen Carriers for Chemical-looping Combustion. *Fuel* **2004**, *83*, 1749–1757.
- (34) Adanez, J.; Abad, A.; Garcia-Labiano, F.; Gayan, P.; de Diego, L. F. Progress in Chemical-looping Combustion and Reforming Technologies. *Prog. Energy Combust.* **2012**, *38*, 215–282.
- (35) Fan, L.-S. *Chemical Looping Systems for Fossil Energy Conversions*, 1st ed.; Wiley-AIChE: Hoboken, NJ, 2010.
- (36) Rohmund, F.; Falk, L. K. L.; Campbell, E. E. B. Iron Catalyzed Growth of Carbon Nanotubes. *AIP Conf. Proc.* **2000**, *544*, 234–237.
- (37) Corbella, B. M.; De Diego, L. F.; García, F.; Adanez, J.; Palacios, J. M. The Performance in a Fixed Bed Reactor of Copper-based Oxides on Titania as Oxygen Carriers for Chemical Looping Combustion of Methane. *Energy Fuels* **2005**, *19*, 433–441.
- (38) Cho, P.; Mattisson, T.; Lyngfelt, A. Carbon Formation on Nickel and Iron Oxide-containing Oxygen Carriers for Chemical-looping Combustion. *Ind. Eng. Chem. Res.* **2005**, *44*, 668–676.
- (39) Bao, J.; Li, Z.; Cai, N. Promoting the Reduction Reactivity of Ilmenite by Introducing Foreign Ions in Chemical Looping Combustion. *Ind. Eng. Chem. Res.* **2013**, *52*, 6119–6128.
- (40) Corbella, B. M.; de Diego, L. F.; García-Labiano, F.; Adanez, J.; Palacios, J. M. Characterization Study and Five-cycle Tests in a Fixed-bed reactor of Titania-supported Nickel oxide as oxygen carriers for the chemical-Looping combustion of methane. *Environ. Sci. Technol.* **2005**, *39*, 5796–5803.
- (41) Kotsionopoulos, N.; Bebelis, S. Electrochemical characterization of the Pt/beta “aEuro” Al<sub>2</sub>O<sub>3</sub> System under Conditions of In situ Electrochemical Modification of Catalytic Activity for Propane Combustion. *J. Appl. Electrochem.* **2010**, *40*, 1883–1891.